Three-dimensional printing of cell-laden bioink for blood vessel tissue engineering: Influence of process parameters and components on cell viability

CONGCONG ZHAN[1], Yasong Hu[1], ANDUO ZHOU[1], SHANFENG ZHANG[1], and Xia Huang[1]

[1]Zhengzhou University

September 26, 2021

Abstract

Three-dimensional (3D) bioprinting is a potential therapeutic method for tissue engineering owing to its ability to prepare cell-laden tissue constructs. The properties of bioink are crucial to accurately control the printing structure. Meanwhile, the effect of process parameters on the precise structure is not nonsignificant. We investigated the correlation between process parameters of 3D bioprinting and the structural response of κ-carrageenan-based hydrogels to explore the controllable structure, printing resolution, and cell survival rate. Small-diameter (<6 mm) gel filaments with different structures were printed by varying the shear stress of the extrusion bioprinter to simulate the natural blood vessel structure. The cell viability of the scaffold was evaluated. The in vitro culture of human umbilical vein endothelium cells (HUVECs) on the κ-carrageenan (kc) and composite gels (carrageenan/carbon nanotube and carrageenan/sodium alginate) demonstrated that the cell attachment and proliferation on composite gels were better than those on pure kc. Our results revealed that the carrageenan-based composite bioinks offer better printability, sufficient mechanical stiffness, interconnectivity, and biocompatibility. This process can facilitate precise adjustment of the pore size, porosity, and pore distribution of the hydrogel structure by optimising the printing parameters as well as realise the precise preparation of the internal structure of the 3D hydrogel-based tissue engineering scaffold. Moreover, we obtained perfused tubular filament by 3D printing at optimal process parameters.

Three-dimensional printing of cell-laden bioink for blood vessel

tissue engineering: Influence ofprocess parameters and components on cell viability

Congcong Zhan [1],Yasong Hu [1], Anduo Zhou [1], Shanfeng Zhang[2], Xia Huang[1,*]

[1] School of Materials Science and Engineering, Zhengzhou University, Zhengzhou, Henan, 450001, P.R. China

[2] School of Basic Medical Science, Zhengzhou University, Zhengzhou, Henan, 450001, P.R. China

** Huang Xia, e-mail: happyhxia@163.com*; Tel.: +86-371-67781590; Fax: +86-371-67781590

ABSTRACT

Three-dimensional (3D) bioprinting is a potential therapeutic method for tissue engineering owing to its ability to prepare cell-laden tissue constructs. The properties of bioink are crucial to accurately control the printing structure. Meanwhile, the effect of process parameters on the precise structure is significant. We investigated the correlation between process parameters of 3D bioprinting and the structural response of κ-carrageenan-based hydrogels to explore the controllable structure, printing resolution, and cell survival rate. Small-diameter (<6 mm) gel filaments with different structures were printed by varying the shear stress of the extrusion bioprinter to simulate the natural blood vessel structure. The cell viability of the

scaffold was evaluated. The *in vitro* culture of human umbilical vein endothelium cells (HUVECs) on the ϰ-carrageenan (kc) and composite gels (carrageenan/carbon nanotube and carrageenan/sodium alginate) demonstrated that the cell attachment and proliferation on composite gels were better than those on pure kc. Our results revealed that the carrageenan-based composite bioinks offer better printability, sufficient mechanical stiffness, interconnectivity, and biocompatibility. This process can facilitate precise adjustment of the pore size, porosity, and pore distribution of the hydrogel structure by optimising the printing parameters as well as realise the precise preparation of the internal structure of the 3D hydrogel-based tissue engineering scaffold. Moreover, we obtained perfused tubular filament by 3D printing at optimal process parameters.

Keywords: 3D bioprinting; cell viability; process parameter; tissue engineering scaffold

Introduction

Recent research on the replacement of large arteries with larger-diameter artificial blood vessels has been comparatively mature[1-2]. However, research on small-diameter artificial blood vessels (of <6-mm diameter) remain formidable and crucial owing to problems such as low compliance in the body and unsatisfactory long-term patency (often resulting in thrombosis and neointimal thickening)[1,3-6]. Cardiovascular tissue engineering is a promising method to improve the traditional vascular graft replacement scaffolds, especially for small-diameter blood vessels[7-9]. Various microfabrication techniques for tissue engineering, such as electrospinning, cell sheet engineering, and mould-casting, have been widely studied to develop complex multi-layered architecture for artificial functional tubular tissues. However, these approaches not only are ineffective in creating the tubular structure with a target-specific mechanical property but also restrict shape-freedom owing to the related technical limitations[10]. The three-dimensional (3D) bioprinting technique is an emerging alternative to overcome the limitations of fabrication in terms of building tubular tissues to mimic the native blood vessel[11-13]. 3D bioprinting has also been utilised for higher-complexity structures with printable bio composite inks containing living cells and natural and synthetic polymers that can be controlled in a spatial position[14]. However, suitable bioinks for producing translationally relevant tissue with complex geometries have not been identified yet.

An ideal bioink simultaneously offers the properties required for 3D bioprinting of complex tissues as well as specific biological cues to support both *in vitro* and *in vivo* tissue maturation. Natural polymer hydrogels with shear-thinning properties are the most widely used materials in bioinks[15-16]. Carrageenan is a class of natural polymers that are extracted from red algae and consist of repeated (1-3)-linked β-D-galactose and (1-4)-linked α-D-galactose units[20-24]. The composition of carrageenan demonstrates similarity with mammalian glycosaminoglycans in a component of the extracellular matrix[25]. In addition, carrageenan inhibits the inflammatory responses because of the presence of negatively charged carboxyl and sulphate groups[26].

However, it is well understood that a single-component hydrogel cannot meet the rigorous requirements of a bioink. Composite hydrogel with multi-component is thus an alternative idea. Alginates are an attractive hydrogel for bioprinting applications as their printability can be changed by altering the polymer density and adding calcium chloride ($CaCl_2$) for cross-linking[17-19]. Furthermore, we can introduce an inorganic component to obtain an ideal bioink. We propose multi-walled carbon nanotubes (MCNTs)[27], with unique electrical, mechanical, and surface properties, for this purpose. MCNTs appear well suited as biomaterials to enhance the properties and functions of medical devices, for example, improving the tracking of cells, sensing of microenvironments, delivering transfection agents, and providing nanostructured surfaces for optimal integration with the host body[28-34], which is not only because of their ability to simulate dimensions of proteins that comprise native tissues using their unique properties but also because of their higher reactivity for cell interactions to improve the cellular functions. Terada et al.[35] proved that rat osteoblast-like MC3T3-E1 cells attached better on MCNTs than on collagens.

In this study, we directly printed small-diameter gel filament with hollow tubular structure through extrusion-based 3D bioprinting instead of the conventional 3D bioprinting method, such as those involving deposition or the use of a roller to simulate the tubular structure of the blood vessel. The feasibility of precise fabrication

of carrageenan/sodium alginate(kc-s) and carrageenan/ MCNTs (kc-c) composite scaffolds was assessed by analysing the printability, shear stress, porosity, and pore size distribution. Printing resolutions of carrageenan-based hydrogels in different printing parameters (such as printing speed and pressure) were presented in the printability maps. Small-diameter gel filaments with different structures are printed by changing the printing parameters of the extrusion bioprinter. We analysed the porosity and pore size distribution of gel filaments by using a scanning electron microscope.

On the other hand, the cell viability of the composite scaffold was evaluated and compared. Then, the biocompatibility of the 3D carrageenan-based composite scaffolds printed with the cells was evaluated with optimised printing parameters by fluorescence staining and imaging. Finally, we analysed the histocompatibility of bioinks with different components under *in vivo* conditions.

Methods and materials

2.1. Configuration of a 3D bioprinter for fabricating gel filaments

We modified the FDM printer for 3D biological printing through syringe loading and mechanical transmission. As shown in Figure 1a, the printer was controlled by the CS10-3 pulse generator and ZD-2HD542 driver. To extrude the biological ink in a stable manner, the 57HB76-401A stepper motor was installed on a customised frame to drive the syringe. The extrusion nozzle was connected to the FDM printer X-Y-Z mobile platform, which could realise the user's customised printing structure. The extrusion velocities range from 0.5 to 10 mL/min out of a 17G (1-mm ID) dispensing needle. Before use, the needle was autoclaved at 121@C, and the printing device was wiped with alcohol and irradiated with ultraviolet light 20-30min.

2.2. Preparation of bioink and cells for 3D bioprinting

Carrageenan, which is mainly composed of ϰ-Carr (Solarbio Inc., Beijing, China), it was mixed at 1.5% w/v concentration with sodium alginate (Solarbio Inc.) solution[36], and the concentration of the alginate solution was fixed at 0.5% w/v, 1% w/v, and 1.5% w/v in this study. MCNTs were purchased from TIMENANO Inc. China and fixed at 0.5% w/v, 1% w/v, and 1.5% w/v). Calcium chloride ($CaCl_2$, Solarbio Inc.) was used as the cross-linking agent for sodium alginate solution. The preparation method of carrageenan composite hydrogel is as follows: (1) kc: ϰ–carrageenan (1.5 g) was dissolved in double-distilled water (100 mL) in a 3-necked round bottom flask and stirred under a constant flow of nitrogen for 4 h. (2) kc-s: carrageenan (1.5 g) and sodium alginate were dissolved in double-distilled water (100 mL) in a 3-necked round bottom flask and stirred under a constant flow of nitrogen gas for 4 h. (3) kc-c: 0.05 g of MCNTs were placed into 50-mL deionised water and subjected to ultrasonic dispersion for 10 min to obtain a carbon nanotube water dispersion system. A certain amount of carbon nanotube dispersion solution was added to the carrageenan solution to obtain a carrageenan/MCNT hydrogel system (carrageenan concentration 1.5% w/v, carbon nanotube concentration 0.01% w/v). All of the prepared hydrogels were aseptically processed before use. Particularly, in this case, we used a high pressure for 1 h and ultraviolet light for 2 h. To prepare the cell-loaded biological ink, we mixed human umbilical vein endothelium cells (HUVECs; Beijing Oligobio, Beijing, China) into a hydrogel for printing.

2.3. Fabrication of gel filaments

Under sterile conditions, the prepared ink was transferred to a printing stock syringe to be extruded through a nozzle with an inner diameter of 1 mm and deposited in an ion cross-linking solution to produce a 3D long gel filament with a diameter of about 1 mm. The printing speed was adjusted to print different types of inks with ideal printability. The gel fibre was soaked in deionised water for 10 min, rinsed, freeze-dried, frozen for 6 h, and then dried for 4 h before use.

2.4. Characterisation of carrageenan-based bioink

2.4.1 Chemical structure of carrageenan-based bioink

The Fourier-transform infrared spectroscopy (FT-IR) spectrum of the kc, kc-s, and kc-c was analysed using Fourier-transformed infrared-attenuated total reflectance (Nicolet Avatar 370, USA). Moreover, the printing

and non-printing FTIR spectra of kc-s and kc-c were analysed. A background spectrum was collected before acquiring the transmission infrared spectra of the samples. All the spectra were between 4000 and 400 cm^{-1}.

2.4.2. Rheological properties of carrageenan-based bioink

The rheological properties of various concentrations of carrageenan and carrageenan composite hydrogel were measured using a rheometer (HR-2, TA Instruments, USA) with a 100-mm round plate at a constant temperature of 37°C. All rheological experiments were performed in triplicate. To assess the rheological properties for optimising the printing parameters, the shear rate sweep test and frequency sweep test were performed. For various shear-thinning materials including carrageenan-based hydrogels, the power-law model has been widely used to analyse the viscoelastic properties. The power-law index (n) and zero viscosity (η_0) were calculated from the shear rate-viscosity curve of the shear rate sweep test in this study. The printing parameters such as the pressure and printing speed were calculated from the power-law index equation, as described below:

$$\eta = \eta_0 \, \gamma^{n-1}$$

where, η is the shear viscosity, γ is the shear rate, and η_0 is the viscosity at the reference shear rate called the zero viscosity (Morrison, 2001; Malkin and Isayev, 2017). The viscosity (η) of the composite hydrogels was assessed using the shear rate sweep test under the shear rate range of 0.1–500 s^{-1}. The frequency sweep test was performed in the angular frequency of 0.1–500 rad/s at a strain in the linear viscoelastic region, where the test was performed without destroying the structure of the sample to assess the storage modulus (G') and the loss modulus (G").

2.4.3. Mechanical testing of carrageenan-based bioink

Mechanical testing was performed by considering the guidelines and standards for elastomers and plastics in tensile measurements (ASTM D412-06a, ASTM D638-14, ISO 37, ISO 527-1,2) as well as the standards for biomedical and regenerative medicine (ASTM F2064-14, ASTM F2900-11, and ASTM F2150-13) relevant for mechanical testing. Bioinks were printed in sheet shape (4-cm length, 1-cm width, and 1.5-mm height) to prevent printing-related stress localisation and inaccurate sample sizes. The sheets were kept in culture medium for 24 h for uniform swelling, and dumb-bell specimens were stamped according to the ISO 527-2-5B standard. The cast bioink sheets (bulk) were similarly stamped. Tension testing was performed using a custom-made testing device with uniaxial hydraulic actuators equipped with 100 N load cells. Custom-made titanium clamps equipped with sandpaper were used for specimen fixation. The tensile specimens were clamped to the retracting probes without preloading, and the stress-strain curves were recorded after a 0.005–0.01 N pre-force was reached.

2.5 Printability of carrageenan-based bioink

The printability of the bioink was analysed at room temperature by comparing the diameter of the printed filament and that of the nozzle (17G; inner diameter 1-mm sterile high precision). In the extrusion printing technique, the accuracy and mechanical properties of the structures were associated with the printed diameter, as determined by Tian et al.[37]:

$$D_s = 2\sqrt{\frac{Q}{\pi V_s}}$$

where, Q, D_s, and V_s are the flow rate of the dispensed biomaterial, printed diameter, and printing speed, respectively. Notably, the extrusion flow rate of a biomaterial is a function of the given operating parameters (such as pressure and temperature), the biomaterial rheological properties (such as viscosity, consistency, and flow index), and geometric parameters (such as needle diameter and length), as given in S1 by Li et al.[38]:

$$Q = \pi \frac{r_1^3 r_0^3}{4} \left[\frac{3n \tan\theta \left(\Delta P + \frac{2\tau_\psi}{\tan\theta \ln \frac{r_1}{r_0}}\right)}{2K\left(r_1^{3n} - r_0^{3n}\right)} \right]^{\frac{1}{n}}$$

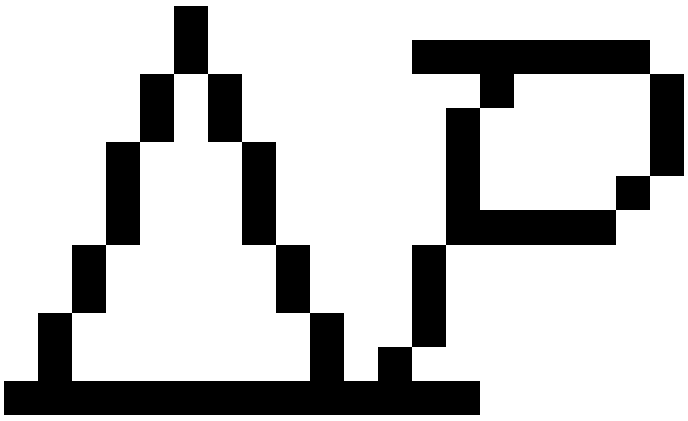

where, r_1 and r_0 are the entrance radius and exit radius of the needle, respectively; P is the pressure exerted and ϑ is the angle between the needle and the deposition surface. In addition, τ_y, n, and K are the yield stress, flow index, and viscosity index, respectively. Note that n and K are related to temperature and ϑ is related to the length of the needle. As previously analysed by extruding-based bioprinting for pressure drop within nozzle diameter D_s and nozzle length L[39], the flow rate can be determined by the following equation:

$$Q = \left(\frac{\pi r_1}{3n+1}\right)\left(\frac{\Delta P}{2\eta_0 L}\right)^{\frac{1}{n}}\left(\frac{D_0}{2}\right)^{\frac{3n+1}{n}}$$

Then, assuming that the printed gel filament is a perfect cylindrical form, the flow rate can be determined by the actual printing speed V_s and printing diameter D_0, as shown below:

$$Q = \frac{V}{t} = \left(\pi\left(\frac{D_s}{2}\right)^2 l\right)\frac{1}{t} = \frac{\pi D_s^2 v_s}{4}$$

where V is the volume of an ideal cylinder, t is the printed time, and l is the printed length. Through these equations, the diameter of the extrusion printing can be obtained under the conditions of determining the rheological performance, printing speed, nozzle diameter, and pressure changes.

2.6. Process parameters and microstructure

Understanding of the shear stress is a crucial factor to consider in the 3D bioprinting process. Studies have demonstrated that shear stress is affected by the diameter of the nozzle, printing pressure, and viscosity of the material to be printed. However, in mechanically driven extrusion-based printing, extrusion speed is another important factor that affects shear stress. When the nozzle diameter and hydrogel viscosity remain unchanged, the shear stress increases with the extrusion printing speed.

We examined the microstructure of hydrogel filament by 3D printing with varied extrusion printing speed and nozzle diameter to freeze the cross-sectional structure formed during extrusion. Then, according to the shear stress gradient at the nozzle, we established a model diagram for pore distribution of the printed gel fibre section.

2.7. Microstructure of samples

After immunofluorescence, the cells on the material were fixed. Next, the samples were washed with phosphate-buffered solution (PBS), dehydrated stepwise with a graded series of ethanol (50, 70, 90, and 100% v/v), and sputter-coated with gold (˜20 nm). The samples were examined at an acceleration of 15 KV by using a scanning electron microscope.

2.8 Nomenclature of samples

To describe the samples, the nomenclature rule was followed:

1) The precursor of hydrogel contain carrageenan named KC;

2) The precursor of hydrogel contain carrageenan and sodium alginate named KC-SA;

3) The precursor of hydrogel contain carrageenan,sodium alginate and carbon nanotube named KC-SA-C; KC-SA-C-0.3 indicate percentage composition of carbon nanotube;

4)KC-SA-C-15kpa indicated sample KC-SA-C-0.3 was printed at 15kpa of printing pressure.

Cell vitality

3.1 Cell culture

HUVECs were purchased from Beijing Oligobio (China). The cells were cultivated in RPMI 1640 medium containing 10% foetal bovine serum (FBS) at 37 @C under a 5% CO_2 atmosphere. The culture medium was refreshed every 2 days. Before mixing with the cells, the composite hydrogel was autoclaved and irradiated with ultraviolet light. The cells were subculture to 80% confluence and mixed with ink at a density of 3×10^4 cell/cm^2 in 24-well plates. The printed structure was then placed in a constant temperature incubator at 37@C under a 5% CO_2 atmosphere. After 6 h of culturing, a fresh medium was replaced to wash out the unadhered cells. The culture medium was changed daily.

3.2. Immunostaining and live/dead staining assay

Live/Dead Staining Assay: The HUVECs were cultured in the RPMI 1640 medium supplemented with 10 v/v% FBS. The cells were resuspended in bioink to achieve a final cell density of 1×10^6cells/mL. Gel filaments of the cell hydrogel suspension were printed into 12-well plates at different pressures (20–40 kpa) by using a nozzle of diameter 1 mm. The cell viability was assessed after printing applying vital-fluorescence-staining using an inverted microscope (DMI6000B; Leica Microsystems, Wetzlar, Germany). The staining solution contained 10 μg mL^{-1} propidium iodide (Solarbio Inc.) and 10 μg mL^{-1} acridine orange (Solarbio Inc.). The number of living and dead cells was counted using the Image J software. Cell viability, (i.e. the ratio between living and dead cells) was plotted against the shear stress, which was calculated for each set of the printing parameters by using the fluid dynamics model.

Immunostaining: The samples were obtained 1, 2, and 3 days after printing. The samples were washed twice with PBS and fixed with 4% paraformaldehyde for 15 min at room temperature, after which all the

samples were rinsed with PBS. The cells were permeated with PBS with 0.1% Triton X (PBS-Tx-0.1%) and sealed in PBS containing 2.5% bovine serum albumin for 30 min to reduce nonspecific background staining. The cells were incubated for 2 h with F-actin (1:500, FITC phalloidin, Sigma, P1951). The cell nuclei were finally labelled using 4-6-Diamidino-2-phenylindol (DAPI, Thermo Fisher Scientific). The cells were rinsed twice and then incubated with DAPI for 10 min under room temperature. After the reaction, the fluorescence microscope was employed to image all the samples.

CCK-8: HUVECs proliferation was assessed using the cell counting kit-8 (CCK-8) method. The CCK-8 was purchased from Solarbio Inc. After the cells are cultured for a certain period (24, 48, and 72 h), they are washed with PBS solution and placed in a new 24-well plate. Then, the CCK-8 reagent was diluted in RPMI 1640 medium at the ratio of 1:10 by adding 200 μL of the diluent to each well and then incubating for 2 h. Next, 100 μL of the diluent from each well was taken and added to a 96-well plate. The absorbance was measured at 450 nm by using a microplate reader (ELX800; BioTek, Vermont, USA).

3.3 Animals and surgical procedure

Adult male Sprague–Dawley rats (weight: 220–250 g) were purchased from the Laboratory Animals Centre, Zhengzhou University. All animal operations and experiments were approved by the Zhengzhou University Animal Care Committees. The rats were anesthetised with 4% isoflurane inhalant anaesthetic and maintained at surgical plane anaesthesia with 2.5% isoflurane throughout the procedure. The samples were assigned to six groups, as follows: freeze-drying (ks-f, kc-f, and k-f) and oven-drying (ks-o, kc-o, and k-o). Following the preparation of the dorsum of the rats, a midline skin incision of approximately 2 cm was made, and the skin and subcutaneous tissues were bluntly dissected. The samples (1.5-cm length, 1.5-cm width, and 0.5-cm height) were subcutaneously implanted into the rats. Following the placement of the samples, the skin and fascia were sutured with 5-0 sutures. Upon completion of the surgical procedure, the inhalant anaesthetic gases were discontinued, and the animal was recovered from anaesthesia. All animals were housed in plastic boxes at a controlled temperature (23 ±2) and were provided *ad libitum* food and water under a standard 12-h on/off light cycle.

Haematoxylin and Eosin Staining

After 2 weeks, the rats were perfused with normal saline, followed by treatment with 4% paraformaldehyde dissolved in 0.1 M PBS to fix the tissues. Then, the tissue samples were collected and post-fixed at 4degC for 8 h. The tissue samples were then dehydrated in 20% and 30% sucrose dissolved in PBS for dehydration, respectively, at 4degC. Next, 10-μm thick slices were subjected to haematoxylin and eosin (H&E) staining. The tissue samples were photographed with a digital camera (HUAWEI P40, China), and the samples were examined and imaged using a high-quality DMI4000 fluorescence microscope (Leica, Germany).

Results and Discussion

4.1 Chemical structure of bioink

As shown in **Figure 2** , the main absorption bands were stretching vibrations of C=O at 1652 cm^{-1} and O-H at 3480 cm^{-1}, which was a broad and redshift due to the formation of H-bond (Figure 2a). After printing, the redshift tendency of kc-sa and kc-SA-C was reduced, indicating that a part of the hydrogen bonds was destroyed during printing (Figure 2b).

4.2. Rheological properties of carrageenan composite hydrogel

The rheological study was performed for composite hydrogel with alginate concentrations of 0.5%, 1.0%, and 1.5%, and with MCNT concentrations of 0.01%, 0.03%, 0.05%, and 1.5%, respectively. A rheological study was performed to evaluate the effects on the viscoelastic properties and the printability of carrageenan composite hydrogel. As shown in Figure 3, all the samples demonstrated shear-thinning properties, which

indicated that bioinks with low viscosity avoid blocking nozzle during printing and cell vitality during cell-laden printing. Shear thinning of composite hydrogel was caused by the destruction of ion cross-linking and rearrangement of the molecular chain by shearing. Moreover, high initial viscosity makes the hydrogel undergo high shear forces during the printing process, which affects the ultimate printability and vitality of the cells. Therefore, we introduced alginate and MCNTs; the initial viscosity of the carrageenan composite hydrogel was decreased with increasing concentrations of alginate and MCNTs, while the shear-thinning properties remained unchanged. The result demonstrated that the introduction of alginate and MCNTs can improve printability and vitality of cells as well as the cytocompatibility of kc-based bioink.

As shown in Figure 4, the initial modulus of kc and composite hydrogel with sa increased slightly. However, the modulus of the composite hydrogel with MCNT and sa increased obviously with the shear frequency. Lower initial modulus endows better survival of cells in the microenvironment. High modulus in a high frequency of hydrogel could avoid the structure disruption and supports the cell well integrity.

The storage modulus (G') of kc was higher than the loss modulus (G") ,gel point(G'= G") was not observed in a range of the test. On the other hand, the gel point was observed in kc-sa and kc-sa-c in the range of measured frequency, which was within the range of shear frequency of the printing nozzle. The results cumulatively implied that kc composite hydrogel was liquid during the process of printing, which ensures that the cells loaded underwent one lower shear force.

4.4. Printability of Carrageenan Composite hydrogel

4.4.1 Printability of carrageenan/sodium alginate hydrogel

The printability of the hydrogel was simulated to present the printing conditions with various printing parameters and to predict the optimal printing parameters based on the measured rheological properties. The printability was calculated as shown in Figure 5(b), with the printing speed of 0–18 mm/s and pressure of 10–40 kPa, by using the equations described above. The cross marks on the printability map represent the actual printing conditions shown in Figure 5(a), and they were labelled with the printing numbers from 1 to 16. Moreover, Figure 5(a) shows the microscopic images of the printed struts at various nozzle velocities (1, 2, 4, and 8 mm/s) and pressures (10, 20, 30, and 40 kPa). The obtained microscopic images were quantitatively analysed to measure the printing resolution and the quality shown in Figure 5(c).

As shown in Figure 5(a), the diameter of the printed gel filament was inversely proportional to the printing rate, while the diameter of printed gel filament decreased with increasing printing rate at low printing pressure (10 kPa). In other words, the samples in the higher printing rate (4 mm/s, 8 mm/s) No. 3 and No. 4 did not acquire an integrated cylindrical structure. At the same printing pressure, the samples No. 1 and No. 2 gel filament were printed with a lower printing speed, resulting in a relatively full cylindrical structure. Thus, unmatched printing speed and printing pressure resulted in insufficient flow filling.

The incomplete shape of gel filament caused by increased printing pressure to 20 kPa existed. The sample No. 8 with 8 mm/s was particularly obvious; however, the uniformity of its diameter and shape integrity was significantly better than that of sample No. 4 (i.e. the same printing speed and lower printing pressure), which demonstrated that the coordination effect of printing pressure and printing speed had an obvious influence on the shape and diameter of the extrusion gel filament and that a higher printing rate cannot be applied with lower printing pressure.

Furthermore, the printability values of samples No. 5, 9, 10, 13, 14, 15, and 16 were greater than 0.5. In Figure 5(b), the printability of samples No. 1, 2, 6, 7, 11, and 12 were assigned according to their print parameters, which matched with the values measured and calculated from the actual printing samples. The results demonstrated that the simulation of printability of kc-sa-1.0 hydrogels were basically accurate. As shown in Figure 5(d), the diameter of the printed gel filament was mainly distributed between 1.0 and 1.8 mm.

4.4.2 Printability of carrageenan/MCNTs hydrogel

As shown in Figure 6, the printability of kc-sa-c-0.3 hydrogel was simulated similar to that of kc-sa-1.0. As for the printability of binary composite hydrogel, the following observations were made:

Printing pressure should be coordinated with the printing rate, and lower pressure with high rate can destroy the integrity of printed structure

The broken line graph of printability lined by a known printing pressure and rate can simulate the printability of unknown pressure and rate.

The above summarised rules apply to the ternary composite hydrogel. In view of the more complex interaction within the ternary composite hydrogel, we added 15 kPa,25 kPa, and 35 kPa pressures for kc-sa-c-0.3.

As shown in Figure 6a, the diameter of the samples No. 5, 9, 10, and 14 was <1.1 mm, that is, the value of printability was <0.1. As shown in Figure 6d, the diameter of the most printed gel filament was 0.8–1.2 mm. Our results demonstrated that the printability of kc-sa-c-0.3 was better than that of kc-sa-1.0.

The printability value of samples No. 13, 18, 19, 22, and 23 was close to zero. These results have been simulated from Figure 6b before printing. These results demonstrated that in the range of the allied printing pressure, the higher is the printing pressure and rate, better is the stability of the filament shape.

4.5. Correlation of the process parameters and microstructure of printing samples

4.5.1. Structural model and process parameters

In an ideal state, shear stress and velocity distribution through the nozzle are shown in Figure (7a). The shear stress is proportional to the radius, and the cut is linear[40]. The flow velocity is parabolic, the centre is the largest, and the wall is zero. In this way, the applied nozzle shear stress gradient distribution affects the printing-related cell damage[41]. Moreover, it can have a different impact on the polymer chain of the gel, thereby affecting the internal structure of the printed fibre.

Considering the shear stress gradient through the nozzle, we established a model diagram of the pore distribution of the printed gel fibre section. The outermost layer of the gel filament had the smallest pore size, followed by the inner layer, with the central layer having the largest pore size. The ideal model diagram of the pore distribution of the printed filament for vessel scaffold is depicted in Figure 7(b).

4.5.2. Core–shell structure of filament

The scanning electron microscopic (SEM) image of the cross-section of the gel filament after freeze-drying is shown in Figure 8; the porous structures were observed in all the samples. The porous structure is important for tissue engineering scaffold. The high porosity provides sufficient surface area to support cell adhesion and growth. Moreover, interconnected networks are considered essential for cell proliferation, nutrition transport, and vascularisation. The pore size of the KC-SA-15kPa scaffold was relatively uniform, with 82% of pore sizes between 80 and 110 μm. With an increase in the printing pressure, delamination occurs along the radius. Coaxial rings near the surface were found to be more compact than those near the axis forming the core–shell structure, which was caused by gradient shear stress and cross-linking. Bioink near-surface was subjected to the maximum shear stress, and the chain segments were arranged regularly, to release more free volume and retaining less water (water in the hydrogel forms ice crystals and sublimates to form pores during freeze-drying). The kc-s scaffold also has different cross-linking degrees between the shell and inner layers, which is in accordance with the diagram shown in Figure 7. The shear stress exhibits a gradient distribution from the shell to the core; therefore, the bridged ions migrate inside the gel, resulting in a lower crosslink density and a higher porosity in the core. The shear stress is isotropic along the circumferential direction, and hence, delamination occurred along the radius.

The core–shell structure was noted in KC-SA-25kPa; the shell layer was dense with small pores, and the core area had large pores. Furthermore, the KC-SA-35kPa scaffold showed a more obvious core–shell structure, with 85% of the pore size between 30 and 70 μm and a large pore present in the centre area.

The SEM images of KC-SA-C-15kPa, KC-SA-C-25kPa, and KC-SA-C-35kPa are shown in Figures 9 and 10. The porous structure of KC-SA-C was similar to that of KC-SA. With increasing printing pressure, the core–shell structure became more obvious, with the central pore of KC-SA-C-0.3 scaffold increasing to 321 μm at 35 kPa of the printing pressure, and the thickness of the shell layer increased obviously with increasing printing pressure (Figure 10).

4.5.3 Perfusable tubular filament by optimal process parameters

The aforementioned results demonstrated that the effect of gradient shear stress and cross-linking was proportional to that of the printing pressure, such that the core pore size and shell layer varied with the printing pressure. As shown in Figure 11, the hollow tubular filament was fabricated, and the inner and outer diameters of the tubular gel filament were 316 μm and 1162 μm, respectively. Small diameter and tubular and porous structure (Figure 10) confirmed that we fabricated small-diameter vascular tissue engineering scaffold by 3D bioprinting.

4.6. Cell vitality of 3D-printing hydrogel filament

4.6.1 Correlation of shear stress and cell vitality

To solve the question of whether it is reasonable to improve printing resolution by increasing the shear stress, evaluating the impact of shear stress on living cells is essential. For this purpose, we investigated the short-term and possible long-term effects of printing-induced shear stress on primary porcine hip arterial endothelial cells (pHAE). We printed pHAE from five independent donors (n = 5) at three different shear stress levels (20, 30, and 40 kPa) and recorded the resultant cell viability (Figure 10a–j). With increasing shear stress, as shown in Figure 12, the average cell viability in the kc composite was significantly decreased from 56.2% (20 kPa) to 42.1% (40 kPa). Nonetheless, the cell viability in kc-s and kc-c seemed unaffected (with >93% average cell viability). Moreover, the viability of the cells in kc-sa-c increased with the printing pressure increasing from 94.7% (20 kPa) to 95.8% (30 kPa). Our results indicated that a higher shear stress may stimulate cell proliferation, as has been reported[42-45]. To understand the effect of shear stress on quantificational cell viability, the distribution of dead cells was assayed using the equal area method. The cross-section of the gel filament was divided into three concentric annulus areas (Figures 12a,1, 2, 3) from the core to the shell. Meanwhile, several dead cells in each area were calculated and averaged. As shown in Figure 12k–m), from the centre (area 1) to the outer (area 3) area, the average cell viability in kc significantly decreased from 60.7% (20 kPa) to 56.3% (20 kPa).A similar conclusion was reached at 30 and 40 kPa (Figure 12k). The average cell viability in kc-sa (Figure 10l) and kc-c (Figure 10m) showed a similar gradient, and the difference in each area was approximately 5%.Due to the gradient distribution of shear stress the cells in the centre layer of the gel filament received the least shearing force, such that the number of dead cells was the least. Secondly, the cells in the middle layer received moderate shearing force. The cells in the outermost layer received the largest shearing force, showing the maximum number of dead cells. The growth of cells exposed to different shear stress levels differed with the printing process. However, to elucidate this phenomenon, further mechanobiological studies with a focus on the intracellular mechanisms in response to shear stress should be conducted.

4.6.2 The effect of printed pressure on cell adhesion and proliferation

In vitro culture of HUVECs in samples: KC-SA-C-15kPa, KC-SA-C-25kPa, and KC-SA-C-35kPa,to assess the effect of printing pressure on the morphology of endothelial cells, the nucleus (blue) and cytoskeleton (green) were stained after endothelial cells laden hydrogels were printed after 24, 48, and 72 h (Figure 13(a–i)).

The proliferation and adhesion of cells increased with an increase in the printing pressure. The cell adhesion in the KC-SA-C-35kPa scaffold was not only more than that in KC-SA-C-15kPa and KC-SA-C-25kPa but also the cell adhesion density and proliferation migration on KC-SA-C-35kPa at the same culture time was significantly better than those under other printing pressures.

Moreover, the diffusion area of cells in the scaffold of other pressures was lower than that in the KC-SA-C-

35kPa scaffold. The cells were distributed more uniformly and showed better interaction and fusion with each other in the KC-SA-C-35kPa scaffold. After 24 h of cell culture, the pseudopod spread area of cells in the KC-SA-C-35kPa scaffold was larger, and the interaction among cells was more obvious after 48 h of culture, indicating a tendency of endothelialisation until 72 h of culture.

Cell adhesion, proliferation, and distribution can be attributed to the microstructures and properties of the scaffold.As shown in the microstructure and of KC-SA-C-0.3(Figure 10), most pores were either incompletely formed or had excessively large pore size in the KC-SA-C-15KPA scaffold, which was not conducive to the initial cell adhesion and subsequent growth parameters. Moreover, the cells grew well in the KC-SA-C-35kPa scaffold, possibly because the KC-SA-C-35kPa scaffold had a porous structure with an outer diameter of 3–50 m and a regular and elliptical distribution; this pore size is conducive to cell growth. The orientation growth of cells was observed in the KC-SA-C-35kPa scaffold, possibly caused by the radial orientation of pores in the printed structure, that is, the shear force was distributed along the radial gradient of the printed structure.

In general, the adhesion cells formed effective adhesion 6 h after growth on the material. Therefore, under similar culture conditions, the cell density in the material after 24-h seeding reflected the cell adhesion ability. The cell density of fluorescent images was statistically analysed using the Image-Pro Plus 6.0 software to evaluate the adhesion ability of HUVECs (Figure 14). As shown in Figure 14, the absorbance of cells in the KC-SA-C-35kPa scaffold was the highest, followed by that in the KC-SA-C-25kPa and then in KC-SA-C-15kPa (lowest). Moreover, the initial adhesion of cells in the KC-SA-C-35kPa scaffold was much higher than that in other scaffolds. After 48 h of culture, the number of cells in the KC-SA-C-35kPa scaffold was the highest, almost covering the entire region, while that in the KC-SA-C-15kPa scaffold was the least, with the trend becoming more obvious after 72 h of culture.

The results together demonstrated that a larger printing pressure is conducive to the uniform distribution of cells, with rapid proliferation and promotion of endothelialisation. Low printing pressure leads to uneven cell distribution, local sedimentation, and aggregation, which are not conducive to cell growth and proliferation.

5. Subcutaneous transplantation of 3D-printed scaffold

Since the *in vivo* assessment of a potential biomaterial is focused on clinical applications, it must be noted that the developed biomaterial should be considered biocompatible without toxicity or any other adverse clinical effects after interaction

within the living systems. During the *in vivo* implantation study, the materials were subcutaneously implanted into the back of the experimental rats under anaesthesia. None of the rats displayed visible signs of inflammation (such as redness, heat, swelling, pain, loss of appetite, and reduced mobility) during the post-implantation period. Surgical sites on all animals appeared normal post-implantation. Upon collecting the samples, no apparent tissue hyperplasia and suppuration were noted in the area surrounding the implant, and no apparent immune rejection reaction was noted between the surrounding tissues and the material (Figure 15).

The tissues collected from animals 2 weeks after the implantation were sectioned and stained with H&E to investigate the cellular inflammatory response to the implanted materials (Figure 16). Comparison between freeze-drying and oven-drying processes revealed no significant difference in the inflammatory status in this study, indicating no effect of the drying preparation method used. The histological sections of the K group were characterised by a large number of inflammatory cells. Some abscess areas were noted. Inflammation was found to be severe, with a large number of neutrophils. The kc group showed marked inflammatory and cellular changes in the epidermis in the presence of neutrophils and mononuclear cells along with oedematous eosinophilic exudate. Moreover, inflammation was nonsignificant or moderate in most sections. The HE-stained sections confirmed the biocompatibility of the ks group with the connective tissues. At day 14, small areas exhibited neutrophil regions. Inflammation was nonsignificant in most sections.

6 Conclusions

A carrageenan-based bioink gel system was established using 1.5% w/v carrageenan to induce rapid gelation of the silk and injectability during printing, allowing the formation of self-standing gel constructs. The printability of carrageenan-based hydrogel was found to improve with increasing concentrations of alginate and MCNTs in the composite hydrogels, and it was found to be the best with the alginate concentration of 1.5% w/v and MCNT concentration of 0.05% w/v. We optimised the printing parameters based on the rheological properties and applied them on kc-s and kc-c composites. Using this approach, we demonstrated excellent structural strength and printability of the carrageenan composite without significant negative effects on the cell viability (>93% average cell viability). With respect to shear force gradients in different areas of the gel filament, we found that despite the different printing pressures, the average cell survival rate of the printed gel also had a certain gradient, and the difference in each area was approximately 5%. This shear force gradient affects the microstructure of the gel filaments and can induce cell growth while responding to the material's response to shear stress. The carrageenan-based bioink system was found to be compatible with HUVECs loaded in the gel matrix, kc-s, and kc-c, supporting better cell growth relative to carrageenan gel. It could achieve precise adjustment of the pore size, porosity, and pore distribution of the hydrogel structure by optimising the printing parameters and realising the precise preparation of the internal structure of the 3D hydrogel-based tissue engineering scaffold. Finally, with the optimal printing conditions, the carrageenan composite hydrogels (kc-s and kc-c) demonstrated the potential as a prospective bioink for fabricating purposes and as a promising 3D-printed scaffold with remarkable mechanical properties, while maintaining the structural and biological activity, in the field of tissue engineering and regenerative medicine.

Acknowledgments

This research was supported by the National Natural Science Foundation of China (No. 51202221).

Statements

The data (figures, tables, and conclusions) used to support the findings of this study are included within the article.

The authors declare that there are no conflicts of interest regarding the publication of this paper.

The study did not utilize animal subjects or tissues. The research in this paper was approved by the Zhengzhou University Life Science Ethic Committee (FWA number: FWA00014064, IRB number: IRB00006861).

Reference

1 D. G. Seifu, A. Purnama, K. Mequanint and D. J. N. R. C. Mantovani, Small-diameter vascular tissue engineering, *Nature Reviews Cardiology* , 2013, **10** , 410-421, DOI: 10.1038/nrcardio.2013.77.

2. Y. Wan, S. Yang, M. Peng, M. Gama and H. J. J. o. M. C. B. Luo, Controllable synthesis of biomimetic nano/submicro-fibrous tubes for potential small-diameter vascular grafts, *Journal of Materials Chemistry B* , 2020, **8** , DOI: 10.1039/D0TB01002B.

3. T. Jungst, I. Pennings, M. Schmitz, A. Rosenberg and D. J. A. F. M. Gawlitta, Heterotypic Scaffold Design Orchestrates Primary Cell Organization and Phenotypes in Cocultured Small Diameter Vascular Grafts, *Advanced Functional Materials* , 2019, DOI: 10.1002/adfm.201905987.

4. G. L. Zhang, D. X. Ke, W. X. Zhao, R. X. Hou, A. Atala, Bioprinting small diameter blood vessel constructs with an endothelial and smooth muscle cell bilayer in a single step, *Biofabrication* , 2020,**12** , 045012 (045014pp), DOI: 10.1088/1758-5090/aba2b6.

5. S. Ravi, Z. Qu and E. L. J. V. Chaikof, Polymeric materials for tissue engineering of arterial substitutes, *Vascular* , 2009,**17 Suppl 1** , S45, DOI: 10.2310/6670.2008.00084.

6. H. Kuang, Y. Wang, Y. Shi, W. Yao and P. J. B. Zhang, Construction and performance evaluation of Hep/silk-PLCL composite nanofiber small-caliber artificial blood vessel graft, *Biomaterials* , 2020,**259** , 120288, DOI: 10.1016/j.biomaterials.2020.120288.

7. S. A. Sell, M. J. Mcclure, K. Garg, P. S. Wolfe and G. L. J. A. D. D. R. Bowlin, Electrospinning of collagen/biopolymers for regenerative medicine and cardiovascular tissue engineering, *Adv Drug Deliv Rev* , 2009, **61** , 1007-1019, DOI: 10.1016/j.addr.2009.07.012.

8. B. D. Plouffe, T. Kniazeva, J. E. Mayer, S. K. Murthy and V. L. J. F. J. Sales, Development of microfluidics as endothelial progenitor cell capture technology for cardiovascular tissue engineering and diagnostic medicine, *The FASEB Journal* , 2009, **23** , 3309-3314, DOI: 10.1096/fj.09-130260.

9. R. Madonna, L. V. Laake, T. Eschenhagen, D. J. Hausenloy and J. S. J. C. R. Hulot, ESC Working Group on Cellular Biology of the Heart: Tissue Engineering and Cell-Based Therapies for Cardiac Repair in Ischemic Heart Disease and Heart Failure, *Cardiovascular Research* , 2019, DOI: 10.1093/cvr/cvz010.

10. H. J. Jeong, H. Nam, J. Jang and S. J. J. B. Lee, 3D Bioprinting Strategies for the Regeneration of Functional Tubular Tissues and Organs, *Bioengineering* , 2020, **7** , DOI:10.3390/bioengineering7020032.

11. H. W. Kang, J. L. Sang, I. K. Ko, C. Kengla and A. J. N. B. Atala, A 3D bioprinting system to produce human-scale tissue constructs with structural integrity, *Nature Biotechnology* , 2016, **34** , 312-319, DOI: 10.1038/nbt.3413.

12. R. Dong, Y. Liu, L. Mou, J. Deng and X. J. J. A. Microfluidics-Based Biomaterials and Biodevices, *Advanced Materials* , 2018, DOI: 10.1002/adma.201805033.

13. Q. Pi, S. Maharjan, R. Parra-Saldivar, N. Hu and W. J. A. M. Jia, Microfluidic Bioprinting: Digitally Tunable Microfluidic Bioprinting of Multilayered Cannular Tissues, *Adv. Mater.,* 2018, **30** , DOI: 10.1002/adma.201870322

14. D. Loessner, C. Meinert, E. Kaemmerer, T. J. Klein, F. Melchels, A. Khademhosseini and D. W. J. N. P. Hutmacher, Functionalization, preparation and use of cell-laden gelatin methacryloyl–based hydrogels as modular tissue culture platforms, *Nature Protocols* , 2016, 11, 727–746, DOI: 10.1038/nprot.2016.037.

15. J. Lou, R. Stowers, S. Nam, Y. Xia and O. J. B. Chaudhuri, Stress relaxing hyaluronic acid-collagen hydrogels promote cell spreading, fiber remodeling, and focal adhesion formation in 3D cell culture,*Biomaterials* , 2017, 11, 213-222.

16. Y. Zhang, J. K. Yu, K. Ren, J. Zuo, J. Ding and X. J. B. Chen, Thermosensitive Hydrogels as Scaffolds for Cartilage Tissue Engineering,*Biomacromolecules* , 2019, DOI: 10.1021/acs.biomac.9b00043.

17. J. Chung, S. Naficy, Z. Yue, R. Kapsa, A. Quigley, S. E. Moulton and G. G. J. B. S. Wallace, Bio-ink properties and printability for extrusion printing living cells, *Biomaterials Science* , 2013,**1** , DOI: 10.1039/C3BM00012E

18. Bin, Duan, Laura, A., Hockaday, Kevin, H., Kang, Jonathan and T. J. J. o. B. M. R. P. A, 3D Bioprinting of heterogeneous aortic valve conduits with alginate/gelatin hydrogels, *Journal of Biomedical Materials Research Part A* , 2012, **101A** , 1255-1264, DOI: 10.1002/jbm.a.34420.

19. C. Ferris, Bio-inks for drop-on-demand cell printing,*Biomaterials Science* , 2013, **1** , 224-230.

20. O. Sipahigil, B. Dortunç and O. K. J. I. J. o. Pharmaceutics, Preparation and in vitro evaluation of verapamil HCl and ibuprofen containing carrageenan beads, *International Journal of Pharmaceutics* , 2001, **228** , 119-128, DOI: 10.1016/S0378-5173(01)00814-6.

21. S. M. Mihaila, A. K. Gaharwar, R. L. Reis, A. P. Marques, M. E. Gomes and A. J. A. H. M. Khademhosseini, Photocrosslinkable Kappa-Carrageenan Hydrogels for Tissue Engineering Applications,*Advanced Healthcare Materials* , 2013, **2** , 895-907, DOI: 10.1002/adhm.201200317.

22. E. G. Popa, M. E. Gomes and L. R. J. B. Rui, Cell delivery systems using alginate–carrageenan hydrogel beads and fibers for regenerative medicine applications, *Biomacromolecules* , 2011, **12** , 3952, DOI: 10.1021/bm200965x.

23. T. Coviello, P. Matricardi, C. Marianecci and F. J. J. o. C. R. O. J. o. t. C. R. S. Alhaique, Polysaccharide hydrogels for modified release formulations, *Journal of Controlled Release* , 2007,**119** , 5-24, DOI: 10.1016/j.jconrel.2007.01.004.

24. P. Cáceres, M. J. Carlucci, E. B. Damonte, B. Matsuhiro and E. A. J. P. Zuniga, Carrageenans from chilean samples of Stenogramme interrupta (Phyllophoraceae): structural analysis and biological activity,*Critical Reviews in Biotechnology* , 2000, **53** , 81-86, DOI: 10.1016/S0031-9422(99)00461-6.

25. M. Rai, A. Yadav and A. Gade, Erratum: Current trends in phytosynthesis of metal nanoparticles (Critical Reviews in Biotechnology 28:4 (277-284)), 2009, DOI: 10.1080/07388550902809566.

26. L. Gasperini, J. F. Mano and R. L. J. J. o. t. R. S. I. Reis, Natural polymers for the microencapsulation of cells, *Journal of The Royal Society Interface* , 2014, **11** , 20140817, DOI: 10.1098/rsif.2014.0817.

27. S. J. N. Iijima, Helical microtubles of graphitic carbon,*Nature* , 1991, **354** , 56-58.

28. Z. Du, X. Feng, G. Cao, Z. She, R. Tan, K. E. Aifantis, R. Zhang and X. J. Li, The effect of carbon nanotubes on osteogenic functions of adipose-derived mesenchymal stem cells in vitro and bone formation in vivo compared with that of nano-hydroxyapatite and the possible mechanism, *Bioactive Materials* , 2021, **6** , 333–345.

29. P. Newman, A. Minett, R. Ellis-Behnke, H. J. N. N. B. Zreiqat and Medicine, Carbon nanotubes: Their potential and pitfalls for bone tissue regeneration and engineering, *Biology and Medicine* , 2013,**9** , 1139-1158, DOI: 10.1016/j.nano.2013.06.001.

30. C. Abdullah, C. L. Azad, R. Ovalle-Robles, A. B. Dalton and N. J. J. A. A. M. I. Plant, Primary Liver Cells Cultured on Carbon Nanotube Substrates for Liver Tissue Engineering and Drug Discovery Applications,*Acs Appl Mater Interfaces* , 2014, **6** , 10373-10380, DOI: 10.1021/am5018489

31. E. R. Aurand, S. Usmani, S. Donato, G. Tromba, M. Prato and L. J. A. F. M. Ballerini, Nanostructures to Engineer 3D Neural-Interfaces: Directing Axonal Navigation toward Successful Bridging of Spinal Segments, *Advanced Functional Materials* , 2018, **28** , 1700550.1700551-1700550.1700512.

32. M. V. Pryzhkova, I. Aria, Q. Cheng, G. M. Harris, X. Zan, M. Gharib and E. J. B. Jabbarzadeh, Carbon nanotube-based substrates for modulation of human pluripotent stem cell fate, *Biomaterials* , 2014, **35** , 5098-5109, DOI: 10.1016/j.biomaterials.2014.03.011.

33. W. Weng, S. He, H. Song, X. Li, L. Cao, Y. Hu, C. Jin, Q. Zhou, H. Peng and J. J. A. N. Su, Aligned Carbon Nanotubes Reduce Hypertrophic Scar via Regulating Cell Behaviour, *Acs Nano* , 2018, DOI: 10.1021/acsnano.7b07439.

34. X. Li, H. Gao, M. Uo, Y. Sato, T. Akasaka, Q. Feng, F. Cui, X. Liu and F. J. J. o. B. M. R. P. A. Watari, Effect of carbon nanotubes on cellular functions in vitro, *Journal of Biomedical Materials Research Part A* , 2009, **91** , 132-139, DOI:10.1002/jbm.a.32203.

35. M. Terada, S. Abe, T. Akasaka, M. Uo and F. W. J. D. M. Journal, Development of a multiwalled carbon nanotube coated collagen dish,*Dental Materials Journal* , 2009, **28** , 82-88, DOI: 10.4012/dmj.28.82.

36. M. H. Kim, W. L. Yong, W. K. Jung, J. Oh and S. Y. J. J. o. t. M. B. o. B. M. Nam, Enhanced rheological behaviors of alginate hydrogels with carrageenan for extrusion-based bioprinting, *Journal of the Mechanical Behavior of Biomedical Materials* , 2019, **98** , 187-194, DOI: 10.1016/j.jmbbm.2019.06.014.

37. X. Y. Tian, M. G. Li, N. Cao, J. W. Li and X. B. J. B. Chen, Characterization of the flow behavior of alginate/hydroxyapatite mixtures for tissue scaffold fabrication, *Biofabrication* , 2009,**1** , 045005, DOI: 10.1088/1758-5082/1/4/045005.

38. M. G. Li, X. Y. Tian and X. B. J. B. Chen, A brief review of dispensing-based rapid prototyping techniques in tissue scaffold fabrication: role of modeling on scaffold properties prediction,*Biofabrication* , 2009, **1** , 032001, DOI:10.1088/1758-5082/1/3/032001.

39. H. Li, S. Liu and L. Li, Rheological study on 3D printability of alginate hydrogel and effect of graphene oxide, *International of journal of bioprinting* , 2016, DOI: 10.18063/IJB.2016.02.007.

40. L. K. Taek, H. Jin, K. Jangho, S. Hoon, C. Pill-Hoon and C. J. J. B. R. I. Hoon, Synergistic effects of orbital shear stress on in vitro growth and osteogenic differentiation of human alveolar bone-derived mesenchymal stem cells, *BioMed Research International* , 2014,**2014** , 316803, DOI:10.1155/2014/316803.

41. T. Distler, A. Sulistio, D. Schneidereit, O. Friedrich and A. R. J. B. Boccaccini, 3D printed oxidized alginate-gelatin bioink provides guidance for C2C12 muscle precursor cell orientation and differentiation via shear stress during bioprinting, *Biofabrication* , 2020, DOI: 10.1088/1758-5090/ab98e4.

42. A. Blaeser, D. D. Campos, U. Puster, W. Richtering, M. M. Stevens and H. J. A. H. M. Fischer, Controlling Shear Stress in 3D Bioprinting is a Key Factor to Balance Printing Resolution and Stem Cell Integrity,*Advanced Healthcare Materials* , 2016, **5** , 326-333, DOI: 10.1002/adhm.201500677.

43. R. Chang, J. Nam and W. J. T. E. P. A. Sun, Effects of dispensing pressure and nozzle diameter on cell survival from solid freeform fabrication-based direct cell writing, *Tissue Engineering Part A* , 2008, **14** , 41-48, DOI: 10.1089/ten.a.2007.0004.

44. J. Ando, H. Nomura and A. J. M. R. Kamiya, The effect of fluid shear stress on the migration and proliferation of cultured endothelial cells,*Microvascular Research* , 1987, **33** , 62-70, DOI: 10.1016/0026-2862(87)90007-01987.

45. K. Nair, M. Gandhi, S. Khalil, K. C. Yan, M. Marcolongo, K. Barbee and W. S. J. B. J. Dr, Characterization of cell viability during bioprinting processes, *Biotechnology Journal* , 2010, **4** , 1168-1177, DOI: 10.1002/biot.200900004.

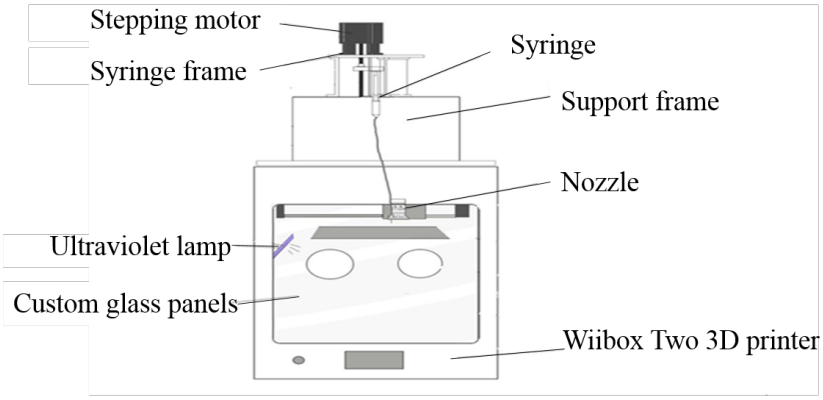

Density of cell gel composites(cells/cm)	$3x10^4$
Diameter of syringe piston (mm)	9.50
Length of the tip (mm)	1.5-3.5
Diameter of the tip (mm)	0.3-1.0
Flow rate (mm'/s)	0.2-20.0

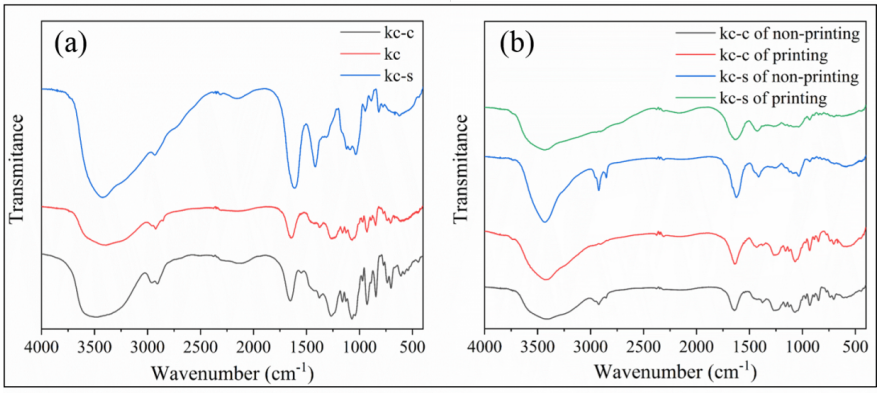

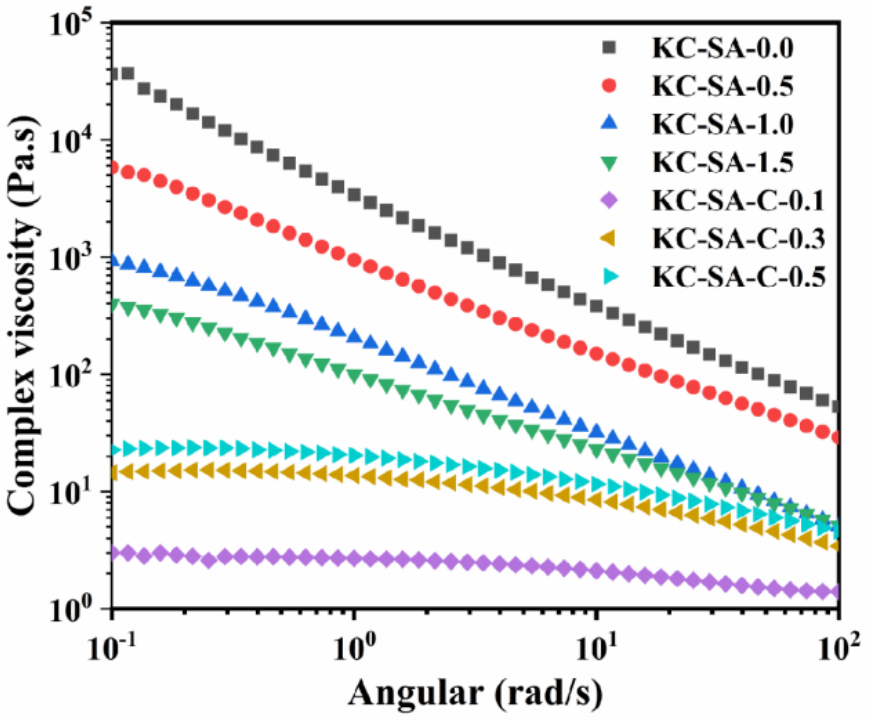

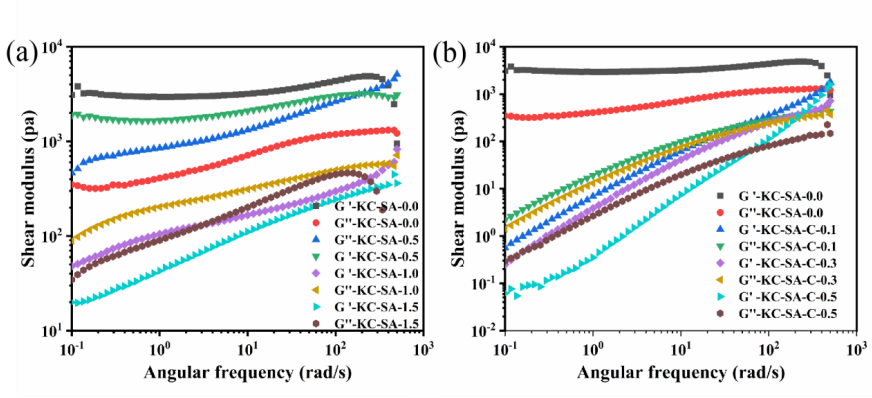

(a)

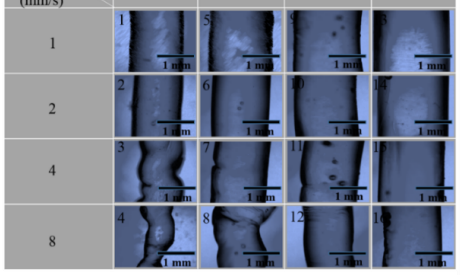

(b)

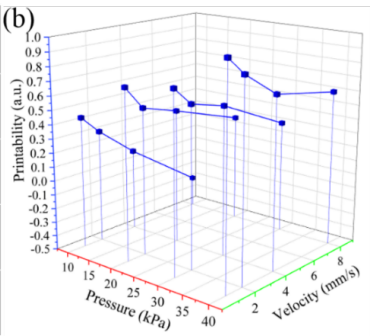

(c)

Pressures (kPa) / Velocity (mm/s)	10	20	30	40
1	1.436 ±0.005	1.710 ±0.017	1.766 ±0.038	2.012 ±0.027
2	1.304 ±0.024	1.542 ±0.024	1.636 ±0.054	1.886±0.032
4	1.088 ±0.046	1.460 ±0.036	1.564 ±0.046	1.706 ±0.029
8	0.756 ±0.066	1.282 ±0.069	1.314 ±0.040	1.608 ±0.056

(d)

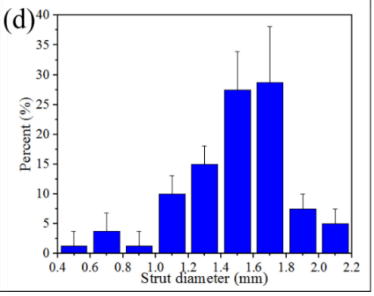

(a)

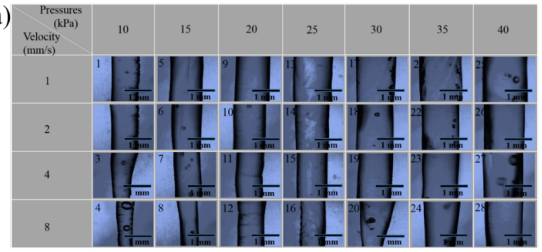

(b)

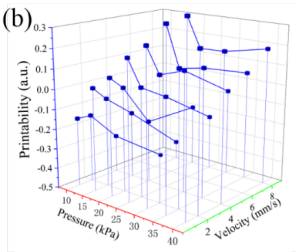

(c)

Pressures (kPa) / Velocity (mm/s)	10	15	20	25	30	35	40
1	0.846 ±0.040	1.018 ±0.028	1.086 ±0.010	1.196 ±0.050	1.266 ±0.037	1.374 ±0.019	1.418 ±0.020
2	0.842 ±0.035	0.948 ±0.037	1.022 ±0.033	1.042 ±0.029	1.120 ±0.057	1.166 ±0.030	1.270±0.068
4	0.690 ±0.083	0.836 ±0.021	0.814 ±0.027	0.962 ±0.031	1.108 ±0.049	1.138 ±0.026	1.230 ±0.041
8	0.490 ±0.031	0.592 ±0.028	0.812 ±0.073	0.780 ±0.036	0.940 ±0.088	1.052 ±0.027	1.188 ±0.017

(d)